Earth Surf. Dynam. Discuss., https://doi.org/10.5194/esurf-2017-38
Manuscript under review for journal Earth Surf. Dynam.
Discussion started: 29 June 2017

Earth Surface Dynamics Discussions
Open Access
EGU

3D topographic monitoring of earth surface deformation using multitemporal UAV photography

François Clapuyt[1], Veerle Vanacker[1], Fritz Schlunegger[2], Kristof Van Oost[1]

[1]Earth and Life Institute, Georges Lemaître Centre for Earth and Climate Research, Université Catholique de Louvain, Belgium.
[2]Institut für Geologie, Universität Bern, Switzerland

Correspondence to: François Clapuyt (francois.clapuyt@uclouvain.be)

Earth Surf. Dynam. Discuss., https://doi.org/10.5194/esurf-2017-38
Manuscript under review for journal Earth Surf. Dynam.
Discussion started: 29 June 2017

Abstract. Accurately assessing geohazards and quantifying landslide risks in mountainous environments gain importance in the context of the on-going global warming. For an in-depth understanding of slope failure mechanisms, accurate monitoring of the mass movement topography at high spatial and temporal resolutions remains essential. The choice of the acquisition framework for high-resolution topographic reconstructions will result from the trade-off between the spatial resolution needed and the extent of the study area. Recent advances in the development of UAV-based (Unmanned Aerial Vehicle) image acquisition combined with Structure-from-Motion (SfM) algorithm for 3D reconstruction makes the UAV-SfM framework a competitive alternative to other high-resolution topographic techniques.

In this study, we test the performance of the UAV-SfM framework to monitor ground surface displacements at very high spatial and temporal resolution, and apply it to the Schimbrig earthflow located in the foothills of the Central Swiss Alps. We produced distinct topographic datasets for three acquisition dates between 2013 and 2015 in order to conduct a comprehensive 3D analysis of the landslide. Therefore, we computed (1) the horizontal and (2) the 3-dimensional surface displacements, and (3) the sediment budget of the hillslope. The multitemporal UAV-SfM based topographic reconstructions allowed us to quantify rates of sediment redistribution and surface movements. Our data show that the Schimbrig earthflow is very active with mean annual horizontal displacement ranging between 6 and 9 meters. The reconstruction of the dynamic topography at very high spatial resolution reveals the internal mechanisms of the earthflow and its complex rotational structure. Although there are major changes in the internal structure of the earthflow in the 2013-2015 period, the sediment budget of the drainage basin is nearly in equilibrium. As a consequence, our data show that the time lag between sediment mobilization by landslides and enhanced sediment fluxes in the river network can be considerable.

Earth Surf. Dynam. Discuss., https://doi.org/10.5194/esurf-2017-38
Manuscript under review for journal Earth Surf. Dynam.
Discussion started: 29 June 2017

1 Introduction

The recent advances in high-resolution topography representation techniques and acquisition platforms, combined with decreasing surveying costs, has led to an increasing availability of topographic datasets over the last decade. High-resolution topographic reconstructions of the earth's landforms are nowadays used for accurate topographic representation and modelling in soil science, volcanology, glaciology, river and coastal morphology (Tarolli, 2014). Meter-accuracy topography has been derived from aerial or satellite optical imagery in the past, and data acquisition is now increasingly achieved using (1) Synthetic Aperture Radar, i.e. SAR, (2) Light Detection and Ranging, i.e. LIDAR, and (3) image-based Structure-from-Motion, i.e. SfM. These techniques are characterized by distinct inherent accuracies and ranges, and can be deployed on either airborne or ground-based platforms. As such, the choice of the acquisition framework for topographic representations will always result from the trade-off between the spatial resolution needed and the extent of the study area (Passalacqua et al., 2015). Terrestrial or satellite SAR and airborne LIDAR (ALS) can cover large areas ranging from 1 km to thousands of kilometres for spacecraft-embedded SAR, with a metric spatial resolution. Ground-based LIDAR, i.e. terrestrial laser scanning (TLS) and image-based Structure-from-Motion can provide topographic surveys at sub-meter spatial resolution outputs for smaller study areas, from the hectare up to a few square-kilometres. Based on pictures taken from a standard camera, 3D topographic reconstructions can cover up to one km-wide study areas if the camera is carried by an Unmanned Aerial Vehicle, i.e. UAV (Immerzeel et al., 2014; Lucieer et al., 2014; Rippin et al., 2015).

The study of geo-hazards benefits from these technological advances for proper monitoring of surface displacements and topographic deformation (Caduff et al., 2015; Jaboyedoff et al., 2012; Joyce et al., 2009; Metternicht et al., 2005; Scaioni et al., 2014). Measurements of surface deformation can be retrieved from chronological sequences of sub-meter resolution topography, where the return period for acquisition and the surveying cost remain important criteria for the selection of the data acquisition platforms. Photogrammetric analyses of aerial photographs or satellite images have frequently been used for landslide monitoring (e.g. Guns and Vanacker, 2014; Sidle and Ochiai, 2006; Vanacker et al., 2003). More recently, SAR images (e.g. Raucoules et al., 2013; Schlögel et al., 2015) and aerial or ground-based LIDAR data (e.g. Blasone et al., 2014; Cavalli et al., 2015; Travelletti et al., 2014; Ventura et al., 2011; Wheaton et al., 2010) are used to retrieve ground surface displacements at high spatial resolution. The use of Structure-from-Motion for temporal analyses is still in its early stages (e.g. Lucieer et al., 2014; Stumpf et al., 2014), even though this technique is now largely applied for single 3D topographic reconstructions and mapping (Eltner et al., 2016). Compared to other topographic acquisition techniques, the UAV-SfM framework is low-cost and flexible in its implementation (Clapuyt et al., 2016), and particularly attractive for survey campaigns in poorly accessible landslide-prone terrain.

This paper aims to quantify ground surface displacements at very-high spatial and temporal resolution, taking benefit from an UAV-SfM framework. We pose that repeated topographic surveys of the slope morphology provide essential data to get an in-depth knowledge of landslide kinematics and dynamics, the hillslope soil residence time in landslide-prone catchments, and to improve landslide hazard assessments. Using the UAV-SfM framework, we produced distinct topographic datasets for a

study site in the Central European Alps of Switzerland for three acquisition dates between 2013 and 2015 and conducted a comprehensive 3D analysis of the landslide by computing (1) the horizontal and (2) the 3-dimensional surface displacements, and (3) the sediment budget of the hillslope. The northern Alpine border, and particularly the foothills of the Central European Alps of Switzerland is prone to slope instabilities, with 6% of its surface area affected by landslide hazards (Lateltin et al., 2005). The outcrop of landslide-prone formations of Flysch and Molasse bedrock having thick interbedded mudstones conditions landslide occurrence. This led local authorities to draw particular attention to georisk management by identifying and assessing landslide hazards (Raetzo et al., 2002) to minimize socio-economic impacts through loss of human life and damage to infrastructure. Climate change is likely to increase landslide hazards in a near future (Crozier, 2010; Huggel et al., 2012). The on-going global warming is characterized by higher mean, minimum and maximum air temperatures and more frequent precipitation events (Cubasch et al., 2013), which has in turn an influence on pre-conditions and triggering mechanisms for landslides (Bennett et al., 2013; Crozier, 2010). The increasing trend in intense precipitation reported for the Northern part of Switzerland is likely to change soil moisture conditions at the Alpine foothills during auttaumn and spring (Seneviratne et al., 2010).

2 Method

2.1 Study area

The study area is the Schimbrig mass movement located in the northern foothills of the Central Swiss Alps, between Bern and Luzern (Fig. 1). This mass movement is categorized as an earthflow, composed of centimetric to decimetric large clasts embedded in a matrix of silt and mud. The mass movement is located in the small, i.e. 4 km² large, Rossloch river catchment, which is part of the Entle river drainage system (Schlunegger et al., 2016a, 2016b). Previous studies on the Schimbrig landslide cover a broad temporal surveying scale from decades (Schwab et al., 2008) to one century (Savi et al., 2013). Our survey complements earlier work in the sense that we will substantially improve the temporal and particularly the spatial resolution of monitoring.

The catchment area is composed of three litho-tectonic units, oriented SW-NE. The upper part, including the Schimbrig ridge culminating at ca. 1,800 meters a.s.l., is formed by a Late Cretacous to Eocene suite of limestones, marls and quartzites, exposed in the Helvetic thrust nappes. The limestones form steep slopes, which are subject to rockfalls (Schlunegger et al., 2016b). Subalpine Flysch deposits are dominant in the intermediate part of the catchment between 1,100 and 1,400 meters a.s.l., where the earthflow is situated. This mass movement covers an area of ca. 45 ha, with a central active part where bare soil is exposed. The lower part of the catchment is covered by conglomerate bedrock knobs of the Subalpine Molasse, which form small resistant conglomerates ridges and constrain the flow direction of the earthflow in its lower segment (Schlunegger et al., 2016b).

Seasonal slip rate variability of the area has been determined by Schwab et al. (2007) based on GPS measurements over a period of 14 months between 2004 and 2005. Slip rates were more intense in early spring and late summer and ranged between 0.1 to 0.25 m/month. During the other periods, slip rates were much lower and ranged between 0 and 0.1 m/month. This displacement pattern has been related to seasonality in soil moisture content. The same authors have not identified an immediate response of this earthflow to rainfall rates. At the decadal scale, volumetric changes of the Schimbrig flow were quantified using classic photogrammetry based on aerial photos from 1962 to 1998 by Schwab et al. (2008). They showed that extreme and episodic changes in slope morphology do not affect the long-term sediment transport to the channel network. Based on dendrogeomorphic analyses, Savi et al. (2013) qualitatively assessed the spatial pattern of geomorphic activity within the Schimbrig area over the last 150 years. Their analyses showed that the earthflow is a source of sediment, and the material mobilized by gravity is slowly supplying material to the drainage network by slow ground movements.

2.2 Data processing

In order to provide a spatial analysis of surface deformation through time, a time-series of very high resolution datasets of 3D point clouds is necessary. The point clouds are generated from overlapping optical images of the Schimbrig area using the Structure-from-Motion algorithm (SfM). Given the high geomorphic activity in the area (Schwab et al., 2008), yearly surveys were planned to accurately capture earthflow movements at high temporal resolution. Three image acquisition campaigns were organised in October 2013, June 2014 and October 2015. Late summer and late spring periods were chosen in order to minimize the effects of vegetation growth.

Image acquisition is done using a UAV platform equipped with a stabilized camera mount, which compensates tilt and roll movements to maintain the fixed orientation of the camera. The latter is a standard small format reflex camera (Canon EOS 550D) with a fixed-focal-length lens (Canon EF 28mm f/2.8 IS USM), equipped with an optical image stabilizer and a high-speed autofocus motorization. The ground surface is surveyed both with nadir-oriented and with a 45°-tilted camera, as the inclusion of oblique images in the SfM algorithm has been shown to decrease systematic errors in topographic reconstruction and to better capture the complex 3D structures (Clapuyt et al., 2016; James and Robson, 2014). The acquisition frequency is set at a rate of one image per two seconds in order to have a high overlap between consecutive images, as high redundancy improves the performance of the SfM algorithm. The output point clouds were georeferenced in post-processing based on ground control points, i.e. georeferencing targets, that were regularly scattered over the fly zone every 25 m, and surveyed with a centimetric accuracy GPS receiver (Clapuyt et al., 2016).

Structure-from-Motion is a computer vision algorithm that uses the set of unoriented overlapping pictures to reconstruct the 3D scene structure without additional a-priori information (Snavely et al., 2006, 2008). The output 3D point cloud is computed in a relative image-based coordinate system, and then georeferenced by matching the real-world coordinates of the georeferencing targets with those expressed in the image-based coordinate system. Based on the list of point pairs, the Helmert transformation parameters, i.e. translation vector, rotation matrix and scaling factor, are computed and applied to the entire

point cloud. The root mean square error computed on the georeferencing target coordinates serves as a measure of the accuracy of the 3D topographic reconstruction.

To quantify internal deformation of the Schimbrig earthflow, three distinct and complementary analyses are realized on the time series of 3D point clouds. First, 3D distances between point clouds are computed to measure the 3D topographic evolution through time, by highlighting zones of erosion, scarp retreat, surface subsidence and zones of bulging and sediment accumulation. The Multiscale Model to Model Cloud Comparison (M3C2) is used to compute 3D distances between point clouds because it directly operates on point clouds without meshing or gridding and provides a confidence interval associated to each distance measurement (Lague et al., 2013), in contrast to other cloud, mesh or raster distance computation techniques. For a set of core points, i.e. either the entire point cloud or a subsample, this method first computes surface normals in 3D. Then, along these normals, the local distance between clouds is the difference between the projection of core points on each cloud. Finally, a spatially variable confidence interval, i.e. a level of detection of local distance between clouds at 95%, is computed based on the registration error, i.e. the accuracy of point cloud georeferencing, and the local roughness of each core point projection along the normals. This confidence interval allows distinguishing statistically significant changes between two point clouds (Lague et al., 2013).

Second, horizontal surface displacements are computed using the COSI-Corr image correlation algorithm (Ayoub et al., 2009; Leprince et al., 2007). Correlation is computed based on a moving window that scans dataset pairs. We used pairs of shaded relief surfaces to detect horizontal displacements. This method is particularly suitable for monitoring slow deformation processes, like the Schimbrig earthflow, with clearly distinguishable surface deformation structures, such as cracks, fissures and scarps. The COSI-Corr algorithm results into horizontal displacements expressed as two layers, i.e. the North-South component and the East-West component, which can be combined to compute the intensity and direction of ground movements. The horizontal displacement analysis is complementary to the above-mentioned 3D analysis of point clouds: the presence of micro-topography and vegetation in the 3D point clouds facilitates the quantification of lateral earth movements using the Cosi-Corr algorithm. As such, the complexity of the earthflow including erosion and accumulation areas and horizontal displacements of the earthflow body is better represented.

Third, the sediment budget is evaluated by computing a digital elevation model of differences (DoD) between the two raster surfaces that were derived from the point clouds. Using the Geomorphic Change Detection software (Wheaton et al., 2010), uncertainties associated to each surface representation and propagation of these errors through DEM of differences are taken into account.

The SfM processing and 3D point cloud georeferencing are performed using the Agisoft Photoscan® software. Point cloud handling has been done with CloudCompare (CloudCompare version 2.6.3, 2016), using the M3C2 plugin. COSI-Corr algorithm has been used as a software module integrated in ENVI. Sediment budgets were computed with the Geomorphic Change Detection software (Wheaton et al., 2010) implemented in ArcGIS. All other data manipulations were carried out with R software and ArcGIS 10.

3 Results

3.1 3D topographic reconstructions

The three topographic reconstructions are not covering the same spatial domain (Table 1; Fig. 2). The flight campaign of June 2014 allowed us to survey the entire Schimbrig earthflow. The 2013 and 2015 flight campaigns are centred on the most active part of the earthflow, but do not cover the entire earthflow due to operational problems encountered during the flight.

Due to these spatial limitations, results are presented: (1) over the spatial intersection of the three datasets ($T_{2013} \cap T_{2014} \cap T_{2015}$), i.e. area of interest named *intersection*, to allow the comparison of absolute values of displacement and volumetric changes over the entire time period (2013-2015), and (2) over the spatial intersection of each time interval ($T_{2013} \cap T_{2014}$ and $T_{2014} \cap T_{2015}$), i.e. area of interest referred to as *interval*, in order to get the most information of each pair of datasets.

The 3D point cloud reconstructions of the Schimbrig earthflow result in a large dataset, with a very high point density of ca. 1,000 to 1,450 points per square meter, which allows to accurately track ground deformation through time. The three topographic reconstructions have similar accuracies, i.e. root mean square errors (Table 1), with horizontal accuracies of 0.23 and 0.20 m, and vertical accuracies of 0.06, 0.05 and 0.08 m. The total error on the topographic reconstructions ranges between 0.20 and 0.24 m. The overall detection limits for ground movements and deformations are derived from error propagation of the RMSE values on the individual topographic constructions given in Table 1.

The detection limits are similar for the two time intervals (Table 2), with a value of 0.31 m for 2013-2014 and 0.30 m for 2014-2015. For further analyses, changes which are smaller than the detection limit of our UAV-SfM framework are not reported.

3.2 Geomorphological map

Based on the time series of very-high resolution digital elevation models, their associated shaded relief surfaces and field observations, a geomorphological map (Fig. 3) of the Schimbrig area is produced.

The Schimbrig earthflow is constrained by stable bedrock ridges covered by trees on the northeastern part, and by relatively stable grasslands on the southwestern part. The main track of the earthflow is from the southeast to the northwest, and it contains two scarps in the upper part that expose up to 25 meters. The earthflow is characterized by a rough surface and a patchwork of vegetated surfaces covered by herbs and small shrubs and bare surfaces where wet and bare soil (silt and mud with embedded clasts) is exposed. The secondary track flows from the northeast to southwest and joins the main track upslope of its accumulation zone.

3.3 3D comparison of earth topography

Distances between 3D point clouds are computed using the Multiscale Model to Model Cloud Comparison algorithm. For each pair of point cloud datasets, a subsample of the first 3D point cloud is taken as the set of core points, with a minimum distance of 0.5 m between points, to avoid extensive computation time. Descriptive statistics are computed on the point cloud distances (Table 3) which were filtered from values under the detection threshold.

The dominance of negative values can be interpreted as predominance of ground subsidence in flat parts or scarp retreat in steeper areas of the earthflow. Contrariwise, positive values are zones of surface bulging in the zones of accumulation or accumulation of debris at the frontal lobe.

3.4 Horizontal displacements

The COSI-Corr image correlation algorithm uses pairs of single-band input to quantify horizontal displacement. A north-directed illumination on the digital elevation models allows to highlight topographic features and ground deformation properly, as well as the presence of low vegetation. Shaded relief surfaces derived from the 3D point clouds (with a spatial resolution of 0.2 m) provided the best results for the correlation analyses. It is important to mention that input data with higher spatial resolution generated incoherent displacement results. Pixels characterized by a signal-to-noise ratio lower than 0.9 or by displacement vectors that are smaller than the detection threshold are discarded for further analyses. To allow comparison between the two time intervals that have a different duration, i.e. 8 versus 17 months, the displacement values are here represented as mean annual displacement values (Table 4).

For the period between October 2013 and June 2014, the fluxes are relatively high and well constrained by stable areas around the earthflow (Fig. 4). The zones that show higher sliding activity are the lower scarp of the earthflow and its adjacent flat slope. The mean annual horizontal displacement for this first period is about 8.9 meters.

The output from the measurements during the second period of interest (2014-2015) shows a slightly different pattern of surface displacements (Fig. 5). The areas with highest displacements are located in the surroundings of the two scarps in the upper part, in the secondary track of the earthflow and in the lower accumulation zone were the frontal lobe spectacularly advanced downslope. In the flatter area between the two scarps, the horizontal movement is less pronounced and the direction of movement is rather diffuse.

When comparing the surface displacements for the two time periods, it is clear that the magnitude of the horizontal displacements is lower in the second period with a mean annual displacement of 5.7 meters.

A comparison with field measurements realized during the flight campaigns in 2013, 2014 and 2015 indicates that the spatial pattern of the horizontal movements that were automatically extracted by the correlation algorithm are generally coherent with field observations. Although the spatial pattern is highly consistent, the absolute displacement of the frontal lobe of the earthflow is not properly captured, as the frontal lobe advanced by ca. 55 meters.

3.5 Sediment budget

Inputs for the sediment budget are the digital elevation models derived from 3D point clouds at the best spatial resolution possible, i.e. 0.04 m. To account for uncertainties related to the UAV-SfM reconstructions, a spatially uniform detection limit has been applied to each input dataset as defined in Table 2.

Over the intersection of the surveyed areas, the best estimate of the volume of deposited sediments is 6,012 m^3, with a minimum and maximum estimate of respectively 4,093 m^3 and 7,932 m^3, for the first period of interest, i.e. between October 2013 and

June 2014 (Table 5; Fig. 6). The volume of eroded sediments is larger, with a best estimate of -11,345 m³, and minimum and maximum estimate of resp. -14,463 m³ and -8,227 m³.

For the first period, there is a net negative change in volume indicating that the removal of material is larger than the accumulation of sliding material for the surveyed surfaces. Field observations reveal a similar pattern. It is important to note that the lower part of the earthflow, where the debris is accumulating in a frontal lobe, is not included in the topographic analyses. Field observations indicate that only a minor part of the sliding material might have been transported to the river network via the Rossloch River.

The sediment budget computed over the second time interval, i.e. between June 2014 and October 2015, for the area of intersection is nearly at equilibrium (Table 5; Fig. 6), with a small negative value for the net volume of difference, i.e. -762 m³. As the minimum and maximum estimates are respectively -4,212 m³ and 2,688 m³, it means that the sliding material that is mobilized by the earthflow accumulated within the area of intersection.

When analysing the internal flow dynamics of the larger sliding area (interval) over the second time interval, it is clear that the sediment budget is slightly positive (Table 5). This analysis now also captures the frontal lobe of the mass movement that bulged and advanced during this time interval. Figure 7 also shows that the upper and lower part of the earthflow are bulging areas, while the intermediate zone is experiencing surface subsidence. The sediment budgets are spatially very consistent with the results on the displacement vectors and distances derived from the point clouds.

4 Discussion

4.1 Application of UAV-SfM framework for landslide monitoring

Using the UAV-SfM framework, three very-high resolution topographic datasets were obtained over a 2-years period that allowed us to quantify accurately the internal dynamics of the earthflow and the sediment redistribution within the study area. First of all, the study shows the efficiency of the UAV-SfM framework to perform natural hazard monitoring at very-high spatial resolution. In fact, the use of an unmanned aerial vehicle equipped with a standard reflex camera is a low-cost and lightweight solution to acquire aerial imagery even in remote and poorly accessible areas. Subsequently, these aerial images can be used to represent landforms in 3D, using the SfM algorithm. The use of the SfM method for topographic surveys offers new perspectives in geomorphology studies (Eltner et al., 2016). This study confirms that the SfM algorithm in itself is robust and can be applied to convert raw image datasets into very-high resolution 3D point clouds. In comparison to other high-resolution topographic methods (Passalacqua et al., 2015; Smith et al., 2015), the UAV-SfM technique, along with terrestrial laser scanning technology, provides the highest spatial resolution of surface reconstructions. Two main advantages of the UAV-SfM framework are its flexibility and low cost, which is convenient for repeated measurements of dynamic environments. In comparison with UAV-SfM, TLS requires careful setup and planning of georeferencing targets and scan locations, to adequately capture the 3D scene of complex topography (Caduff et al., 2015). In this study case, a one-year time interval between surveys was suitable to capture the internal dynamics of the earthflow. We recognize that other natural hazards

may require a higher frequency of measurements, which can easily be achieved using UAVs. The drawback of the UAV-SfM framework is the need for the UAV platform to acquire aerial pictures. The use of UAVs is now increasingly subjected to more stringent regulations, including a pilot license, UAV registration, and insurance certificates. Moreover, UAV flights are only possible under optimal meteorological conditions, and wind and rain may be a limiting factor in mountainous areas. Schimbrig earthflow monitoring.

4.2 Schimbrig earthflow monitoring

Post-processing of the time-series of digital surface models provides 3D comparisons of surfaces, horizontal displacements and sediment budgets that allow us to monitor the internal dynamics of the mass movement at very high spatial and temporal resolution. By combining the three single results, which may seem redundant at first sight, it is possible to quantify the magnitude and rate of sediment redistribution and surface movements within the area affected by the Schimbrig earthflow and to capture the internal mechanisms of the earthflow (Fig. 8).

As such, the very-high resolution topographic reconstructions allow to analyse the spatio-temporal evolution of earthflow-prone terrain, and to go beyond conventional survey methods and expert knowledge (Schwab et al., 2008). Our data show that the entire body of the earthflow is sliding, but that there exist strong differences in internal deformation and flow velocities within the sliding material. By combining the results from the 3D comparison between the point clouds and the DEM of differences, it is possible to map the succession of ground surface subsidence and bulging areas over the three-year period. Notwithstanding the short monitoring interval, the pattern of internal deformation of the earthflow changed its configuration (Fig. 8). Between October 2013 and June 2014, the earthflow had a succession of three nested rotational units. In the upper part of the study area, two steep scarps are present. These active scarps control the downward movement of two tilted blocks (see Fig. 3). The location of the two main scarps advances by ca. 8 m during the 2013-2014 period. A third rotational unit is larger: it is defined by a steep scarp located in the middle part of the earthflow, and extends over the lower and flatter part of the earthflow down the frontal lobe.

During the second period of monitoring, i.e. between June 2014 and October 2015, two rotational units can clearly be distinguished, i.e. a small upper block that is confined above the upper active scarp, and a larger heterogeneous sliding mass that extends down to the frontal lobe of the earthflow. Unlike the first period of interest, the lower erosional scarp is not active, and there is no distinction between the second and third part of the sliding mass.

The very high resolution spatio-temporal analyses demonstrate that the Schimbrig earthflow has been very active over the monitoring period. Results from the image correlation algorithm highlight the strong internal redistribution of sliding material within the earthflow, and rapid changes in the spatial pattern of displacement vectors. The mean annual horizontal displacements are large with values of ca. 9 m between October 2013 and June 2014 and ca. 6 m between June 2014 and October 2015. This is partly explained by the fact that the central part of the earthflow is advancing toward the foot of the earthflow between October 2013 and June 2014, and this advance is accompanied by surface subsidence along the main track.

This phase is followed by bulging in the accumulation zone, and a strong advance of the frontal lobe of the landslide over a distance of ca. 55 m.

Notwithstanding the strong internal deformation of the sliding material, there is no net effect on the sediment flux at the outlet of the Rossloch River. Our data show that the overall sediment budget of the earthflow is nearly in equilibrium. After the major surge that occurred in 1994, the earth surface lowered by ca. 12 m in the central track of the earthflow (Schwab et al., 2008). More than 20 years later, the earthflow shows strong internal deformation that is related to the re-adjustment and self-reorganisation of the sliding material after the 1994 surge event. This suggests that phases of enhanced earthflow kinematics are not necessarily leading to enhanced sediment export to the fluvial system, because of the time delay between successive phases of earthflow reactivation and the sediment export from the catchment.

5 Conclusion

The UAV-SfM framework is increasingly applied in geomorphology to accurately capture the topography of given scenes. As it is low cost and flexible in its implementation, and particularly suitable for surveying dynamic environments in poorly accessible terrain, we used this methodology to quantify ground surface displacements of the Schimbrig earthflow, located at the foothills of the Central Swiss Alps, at very-high spatial and temporal resolution. Based on three topographic reconstructions between autumn 2013 and 2015, we were able to conduct a comprehensive 3D analysis of the landslide by combining the horizontal and the 3-dimensional surface displacements, and the sediment budget of the hillslope.

Results confirm that the Schimbrig earthflow is very active with mean annual horizontal displacements between 6 and 9 m. Besides, we showed that the sediment budget of the hillslope is nearly at equilibrium. In fact, the earthflow has experienced a major sediment pulse more than 20 years ago, and is still re-adjusting to this new setting. Therefore, we suggest that the time lag between activation of landslides and the enhanced sediment fluxes in the river system can be considerable. Post-processing of the time-series of digital surface models provides 3D comparisons of surfaces, horizontal displacements and sediment budgets that allow us to reconstruct the internal dynamics of the earthflow and highlight its complex rotational movement. Finally, this study complements previous work in the area that was realized with traditional survey methods, and allows to quantify the hillslope soil residence time in landslide-prone catchments.

Competing interests

The authors declare that they have no conflict of interest.

Acknowledgements

Authors would like to thank Emilien Aldana Jague and Marco Bravin for the help and the support during test flights with the UAVs used to acquire aerial images. We would also like to acknowledge Romain Delunel from Bern University for its availability and help regarding the handling of the GPS used to survey ground control points during field work.

Low-cost research is also possible thanks to the developers making their software freely available: Dimitri Lague and Nicolas Brodu for M3C2 algorithm; the COSI-Corr development team, from Caltech (California Institute of Technology) Tectonics Observatory; Joe Wheaton and colleagues for the Geomorphic Change Detection software.

References

Anon: CloudCompare version 2.6.3 [GPL Software], [online] Available from: http://www.cloudcompare.org/, 2016.

Ayoub, F., Leprince, S. and Avouac, J.-P.: Co-registration and correlation of aerial photographs for ground deformation measurements, ISPRS J. Photogramm. Remote Sens., 64(6), 551–560, doi:10.1016/j.isprsjprs.2009.03.005, 2009.

Bennett, G. L., Molnar, P., McArdell, B. W., Schlunegger, F. and Burlando, P.: Patterns and controls of sediment production, transfer and yield in the Illgraben, Geomorphology, 188, 68–82, doi:10.1016/j.geomorph.2012.11.029, 2013.

Blasone, G., Cavalli, M., Marchi, L. and Cazorzi, F.: Monitoring sediment source areas in a debris-flow catchment using terrestrial laser scanning, Catena, 123, 23–36, doi:10.1016/j.catena.2014.07.001, 2014.

Caduff, R., Schlunegger, F., Kos, A. and Wiesmann, A.: A review of terrestrial radar interferometry for measuring surface change in the geosciences, Earth Surf. Process. Landforms, 40(2), 208–228, doi:10.1002/esp.3656, 2015.

Cavalli, M., Goldin, B., Comiti, F., Brardinoni, F. and Marchi, L.: Assessment of erosion and deposition in steep mountain basins by differencing sequential digital terrain models, Geomorphology, (2015), doi:10.1016/j.geomorph.2016.04.009, 2015.

Clapuyt, F., Vanacker, V. and Van Oost, K.: Reproducibility of UAV-based earth topography reconstructions based on Structure-from-Motion algorithms, Geomorphology, 260, 4–15, doi:10.1016/j.geomorph.2015.05.011, 2016.

Crozier, M. J.: Deciphering the effect of climate change on landslide activity: A review, Geomorphology, 124(3–4), 260–267, doi:10.1016/j.geomorph.2010.04.009, 2010.

Cubasch, U., Wuebbles, D., Chen, D., Facchini, M. C., Frame, D., Mahowald, N. and Winther, J.-G.: Introduction in Climate Change 2013, Intergov. Panel Clim. Chang. 2013 Phys. Sci. Basis. Contrib. Work. Gr. I to Fifth Assess. Rep. Intergov. Panel Clim. Chang., 119–158, doi:10.1017/CBO9781107415324.007, 2013.

Eltner, A., Kaiser, A., Castillo, C., Rock, G., Neugirg, F. and Abellan, A.: Image-based surface reconstruction in geomorphometry – merits, limits and developments of a promising tool for geoscientists, Earth Surf. Dyn., 4, 359–389, doi:10.5194/esurf-4-359-2016, 2016.

Guns, M. and Vanacker, V.: Shifts in landslide frequency–area distribution after forest conversion in the tropical Andes, Anthropocene, 6, 75–85, doi:10.1016/j.ancene.2014.08.001, 2014.

Huggel, C., Clague, J. J. and Korup, O.: Is climate change responsible for changing landslide activity in high mountains?, Earth Surf. Process. Landforms, 37(1), 77–91, doi:10.1002/esp.2223, 2012.

Immerzeel, W. W., Kraaijenbrink, P. D. a., Shea, J. M., Shrestha, A. B., Pellicciotti, F., Bierkens, M. F. P. and de Jong, S. M.: High-resolution monitoring of Himalayan glacier dynamics using unmanned aerial vehicles, Remote Sens. Environ., 150, 93–103, doi:10.1016/j.rse.2014.04.025, 2014.

Jaboyedoff, M., Oppikofer, T., Abellán, A., Derron, M.-H., Loye, A., Metzger, R. and Pedrazzini, A.: Use of LIDAR in landslide investigations: a review, Nat. Hazards, 61(1), 5–28, doi:10.1007/s11069-010-9634-2, 2012.

James, M. R. and Robson, S.: Mitigating systematic error in topographic models derived from UAV and ground-based image

networks, Earth Surf. Process. Landforms, 3609, n/a-n/a, doi:10.1002/esp.3609, 2014.

Joyce, K. E., Belliss, S. E., Samsonov, S. V., McNeill, S. J. and Glassey, P. J.: A review of the status of satellite remote sensing and image processing techniques for mapping natural hazards and disasters, Prog. Phys. Geogr., 33(2), 183–207, doi:10.1177/0309133309339563, 2009.

Lague, D., Brodu, N. and Leroux, J.: Accurate 3D comparison of complex topography with terrestrial laser scanner: Application to the Rangitikei canyon (N-Z), ISPRS J. Photogramm. Remote Sens., 82, 10–26, doi:10.1016/j.isprsjprs.2013.04.009, 2013.

Lateltin, O., Haemmig, C., Raetzo, H. and Bonnard, C.: Landslide risk management in Switzerland, Landslides, 2(4), 313–320, doi:10.1007/s10346-005-0018-8, 2005.

Leprince, S., Barbot, S., Ayoub, F. and Avouac, J.: Automatic and precise orthorectification, coregistration, and subpixel correlation of satellite, images, application to ground deformation measurements, , 45(6), 1529–1558, 2007.

Lucieer, A., de Jong, S. M. and Turner, D.: Mapping landslide displacements using Structure from Motion (SfM) and image correlation of multi-temporal UAV photography, Prog. Phys. Geogr., 38(1), 97–116, doi:10.1177/0309133313515293, 2014.

Metternicht, G., Hurni, L. and Gogu, R.: Remote sensing of landslides: An analysis of the potential contribution to geo-spatial systems for hazard assessment in mountainous environments, Remote Sens. Environ., 98(2–3), 284–303, doi:10.1016/j.rse.2005.08.004, 2005.

Passalacqua, P., Belmont, P., Staley, D. M., Simley, J. D., Arrowsmith, J. R., Bode, C. a., Crosby, C., DeLong, S. B., Glenn, N. F., Kelly, S. a., Lague, D., Sangireddy, H., Schaffrath, K., Tarboton, D. G., Wasklewicz, T. and Wheaton, J. M.: Analyzing high resolution topography for advancing the understanding of mass and energy transfer through landscapes: A review, Earth-Science Rev., 148, 174–193, doi:10.1016/j.earscirev.2015.05.012, 2015.

Raetzo, H., Lateltin, O., Bollinger, D. and Tripet, J. P.: Hazard assessment in Switzerland - Codes of practice for mass movements, Bull. Eng. Geol. Environ., 61(3), 263–268, doi:10.1007/s10064-002-0163-4, 2002.

Raucoules, D., de Michele, M., Malet, J. P. and Ulrich, P.: Time-variable 3D ground displacements from high-resolution synthetic aperture radar (SAR). application to La Valette landslide (South French Alps), Remote Sens. Environ., 139, 198–204, doi:10.1016/j.rse.2013.08.006, 2013.

Rippin, D. M., Pomfret, A. and King, N.: High resolution mapping of supra-glacial drainage pathways reveals link between micro-channel drainage density, surface roughness and surface reflectance, Earth Surf. Process. Landforms, 40(10), 1279–1290, doi:10.1002/esp.3719, 2015.

Savi, S., Schneuwly-Bollschweiler, M., Bommer-Denns, B., Stoffel, M. and Schlunegger, F.: Geomorphic coupling between hillslopes and channels in the Swiss Alps, Earth Surf. Process. Landforms, 38(9), 959–969, doi:10.1002/esp.3342, 2013.

Scaioni, M., Longoni, L., Melillo, V. and Papini, M.: Remote -sensing for landslide investigations: An overview of recent achievements and perspectives, Remote Sens., 6(10), 9600–9652, doi:10.3390/rs6109600, 2014.

Schlögel, R., Doubre, C., Malet, J. P. and Masson, F.: Landslide deformation monitoring with ALOS/PALSAR imagery: A D-

InSAR geomorphological interpretation method, Geomorphology, 231, 314–330, doi:10.1016/j.geomorph.2014.11.031, 2015.

Schlunegger, F., Jost, J., Grünig, A. and Trüssel, M.: Erläuterungen, Geologischer Atlas der Schweiz, Kartenblatt 1169 Schüpfheim 1:25'000, Bundesamt für Landestopographie swisstopo, 107pp, 2016a.

Schlunegger, F., Anspach, O., Bieri, B., Böning, P., Kaufmann, Y., Lahl, K., Lonschinski, M., Mollet, H., Sachse, D., Schubert, C., Stöckli, G. and Zander, I.: Geologische Karte der Schweiz, Kartenblatt 1169 Schüpfheim 1:25'000, Bundesamt für Landestopographie swisstopo, 2016b.

Schwab, M., Läderach, C., Rieke-Zapp, D. and Schlunegger, F.: Slip rates variability and sediment mobilization on a shallow landslide in the northern Swiss Alps, Swiss J. Geosci., 100(2), 281–292, doi:10.1007/s00015-007-1218-0, 2007.

Schwab, M., Rieke-Zapp, D., Schneider, H., Liniger, M. and Schlunegger, F.: Landsliding and sediment flux in the Central Swiss Alps: A photogrammetric study of the Schimbrig landslide, Entlebuch, Geomorphology, 97(3–4), 392–406, doi:10.1016/j.geomorph.2007.08.019, 2008.

Seneviratne, S. I., Corti, T., Davin, E. L., Hirschi, M., Jaeger, E. B., Lehner, I., Orlowsky, B. and Teuling, A. J.: Investigating soil moisture-climate interactions in a changing climate: A review, Earth-Science Rev., 99(3–4), 125–161, doi:10.1016/j.earscirev.2010.02.004, 2010.

Sidle, R. C. and Ochiai, H.: Landslides: Processes, Prediction, and Land Use, Wiley., 2006.

Smith, M. W., Carrivick, J. L. and Quincey, D. J.: Structure from motion photogrammetry in physical geography, Prog. Phys. Geogr., 40(2), 247–275, doi:10.1177/0309133315615805, 2015.

Snavely, N., Seitz, S. M. and Szeliski, R.: Photo tourism: Exploring Photo Collections in 3D, ACM Trans. Graph., 25(3), 835–846, doi:10.1145/1141911.1141964, 2006.

Snavely, N., Seitz, S. M. and Szeliski, R.: Modeling the World from Internet Photo Collections, Int. J. Comput. Vis., 80(2), 189–210, doi:10.1007/s11263-007-0107-3, 2008.

Stumpf, A., Malet, J.-P., Allemand, P., Pierrot-Deseilligny, M. and Skupinski, G.: Ground-based multi-view photogrammetry for the monitoring of landslide deformation and erosion, Geomorphology, 231, 130–145, doi:10.1016/j.geomorph.2014.10.039, 2014.

Tarolli, P.: High-resolution topography for understanding Earth surface processes: Opportunities and challenges, Geomorphology, 216, 295–312, doi:10.1016/j.geomorph.2014.03.008, 2014.

Travelletti, J., Malet, J.-P. and Delacourt, C.: Image-based correlation of Laser Scanning point cloud time series for landslide monitoring, Int. J. Appl. Earth Obs. Geoinf., 32(0), 1–18, doi:http://dx.doi.org/10.1016/j.jag.2014.03.022, 2014.

Vanacker, V., Vanderschaeghe, M., Govers, G., Willems, E., Poesen, J., Deckers, J. and De Bievre, B.: Linking hydrological, infinite slope stability and land-use change models through GIS for assessing the impact of deforestation on slope stability in high Andean watersheds, Geomorphology, 52(3–4), 299–315, doi:10.1016/S0169-555X(02)00263-5, 2003.

Ventura, G., Vilardo, G., Terranova, C. and Sessa, E. B.: Tracking and evolution of complex active landslides by multi-temporal airborne LiDAR data: The Montaguto landslide (Southern Italy), Remote Sens. Environ., 115(12), 3237–3248,

doi:10.1016/j.rse.2011.07.007, 2011.

Wheaton, J. M., Brasington, J., Darby, S. E. and Sear, D. a.: Accounting for uncertainty in DEMs from repeat topographic surveys: improved sediment budgets, Earth Surf. Process. Landforms, 35, 136–156, doi:10.1002/esp.1886, 2010.

5

Earth Surf. Dynam. Discuss., https://doi.org/10.5194/esurf-2017-38
Manuscript under review for journal Earth Surf. Dynam.
Discussion started: 29 June 2017

Figures

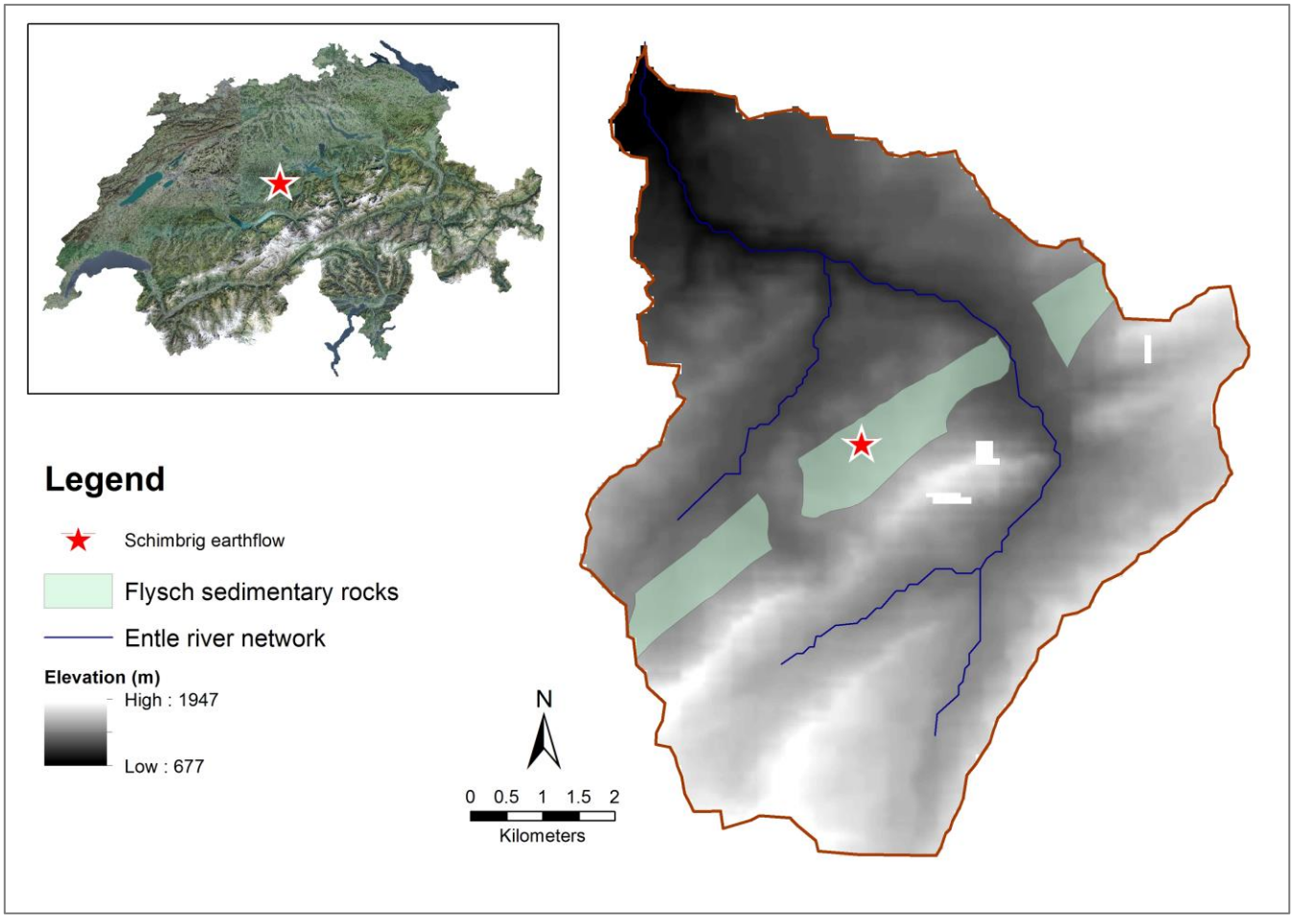

Figure 1: Location of the Schimbrig landslide in Switzerland (inset) and in the Entle river watershed.

Earth Surf. Dynam. Discuss., https://doi.org/10.5194/esurf-2017-38
Manuscript under review for journal Earth Surf. Dynam.
Discussion started: 29 June 2017

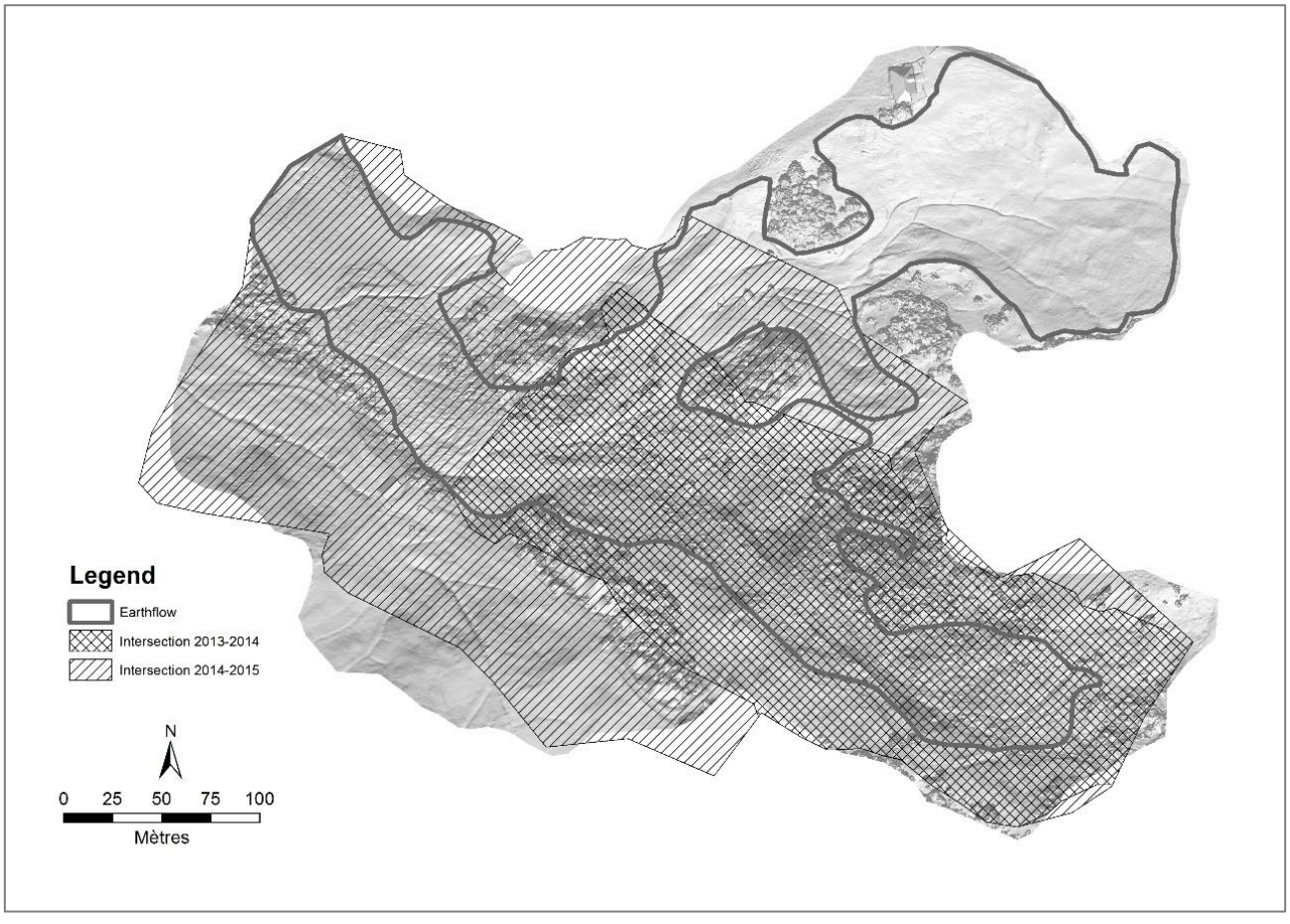

Figure 2: Intersections of point cloud datasets for the 2013-2014 and 2014-2015 time intervals.

Earth Surf. Dynam. Discuss., https://doi.org/10.5194/esurf-2017-38
Manuscript under review for journal Earth Surf. Dynam.
Discussion started: 29 June 2017

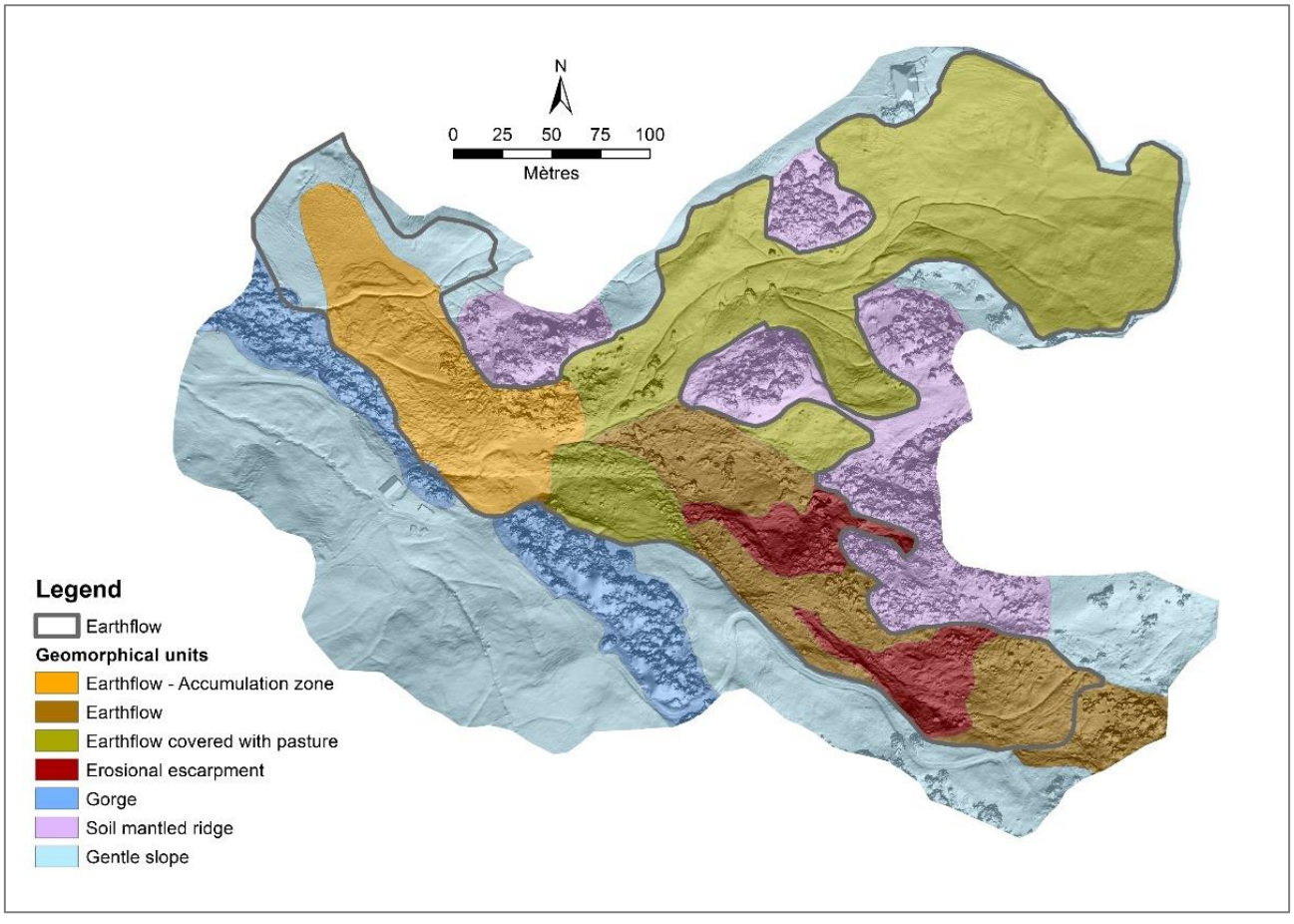

Figure 3: Geomorphological map of the study area.

Earth Surf. Dynam. Discuss., https://doi.org/10.5194/esurf-2017-38
Manuscript under review for journal Earth Surf. Dynam.
Discussion started: 29 June 2017

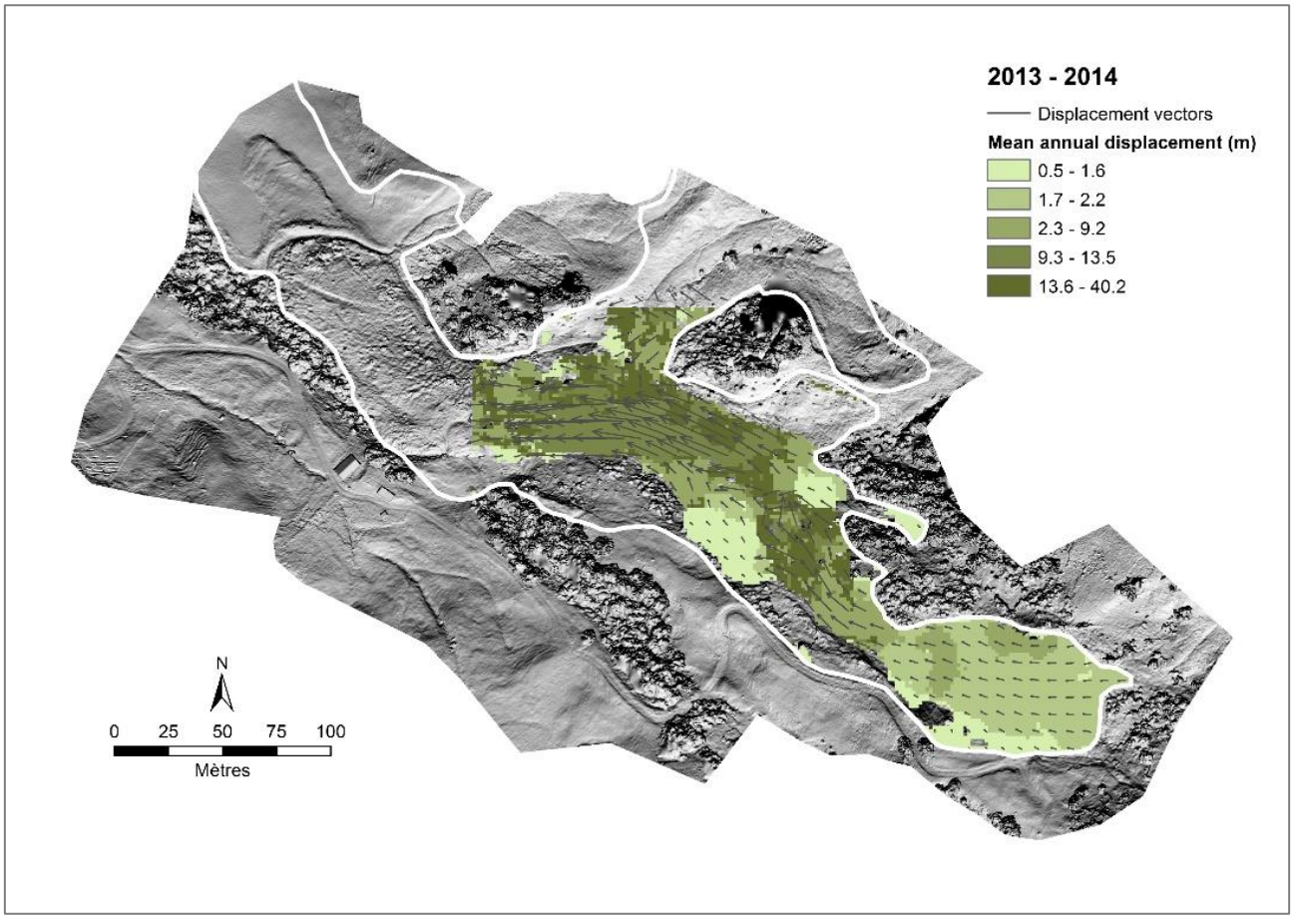

Figure 4: Surface displacements for 2013-2014 using the COSI-Corr algorithm.

Earth Surf. Dynam. Discuss., https://doi.org/10.5194/esurf-2017-38
Manuscript under review for journal Earth Surf. Dynam.
Discussion started: 29 June 2017

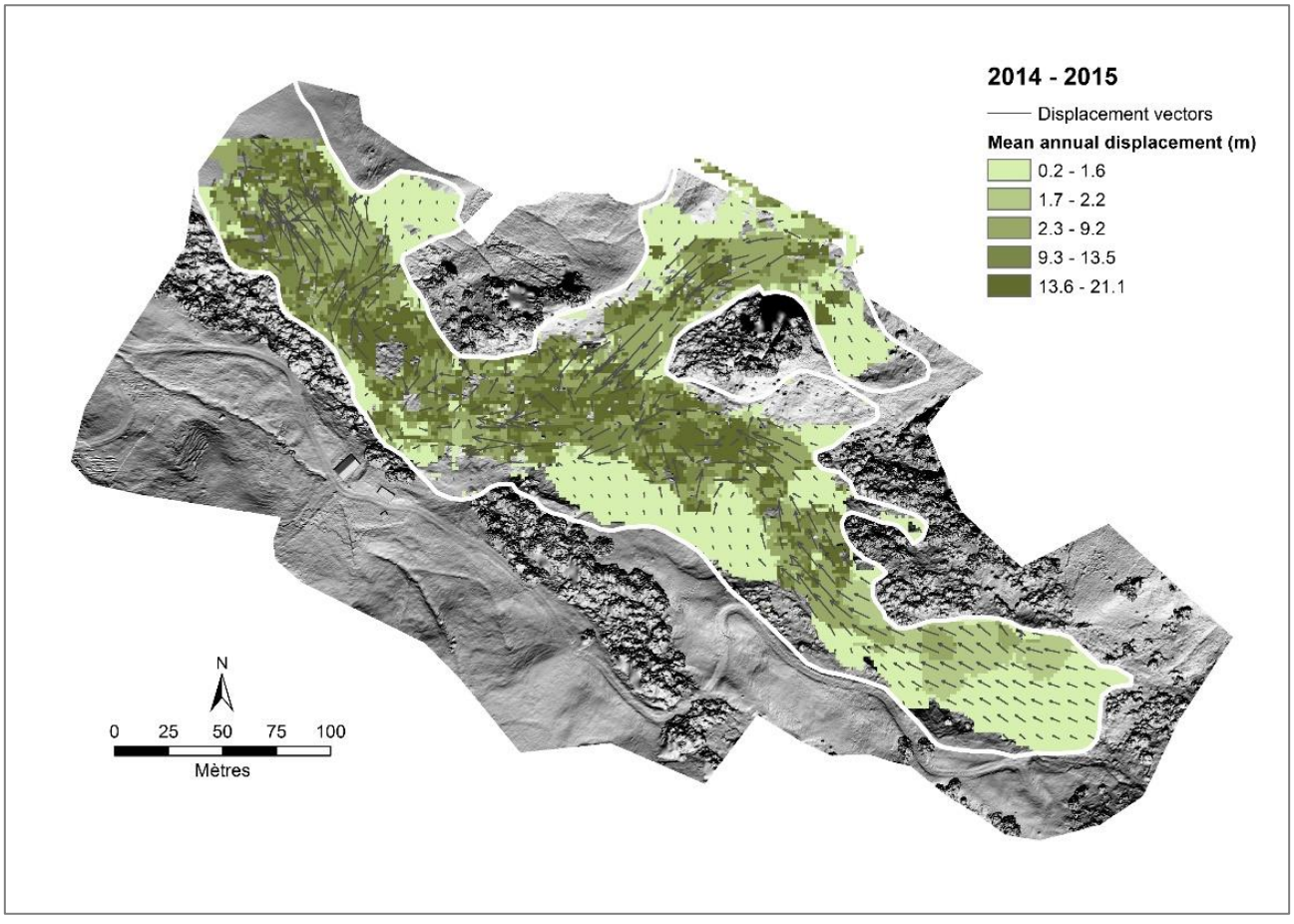

Figure 5: Surface displacements for 2014-2015 using the COSI-Corr algorithm.

Earth Surf. Dynam. Discuss., https://doi.org/10.5194/esurf-2017-38
Manuscript under review for journal Earth Surf. Dynam.
Discussion started: 29 June 2017

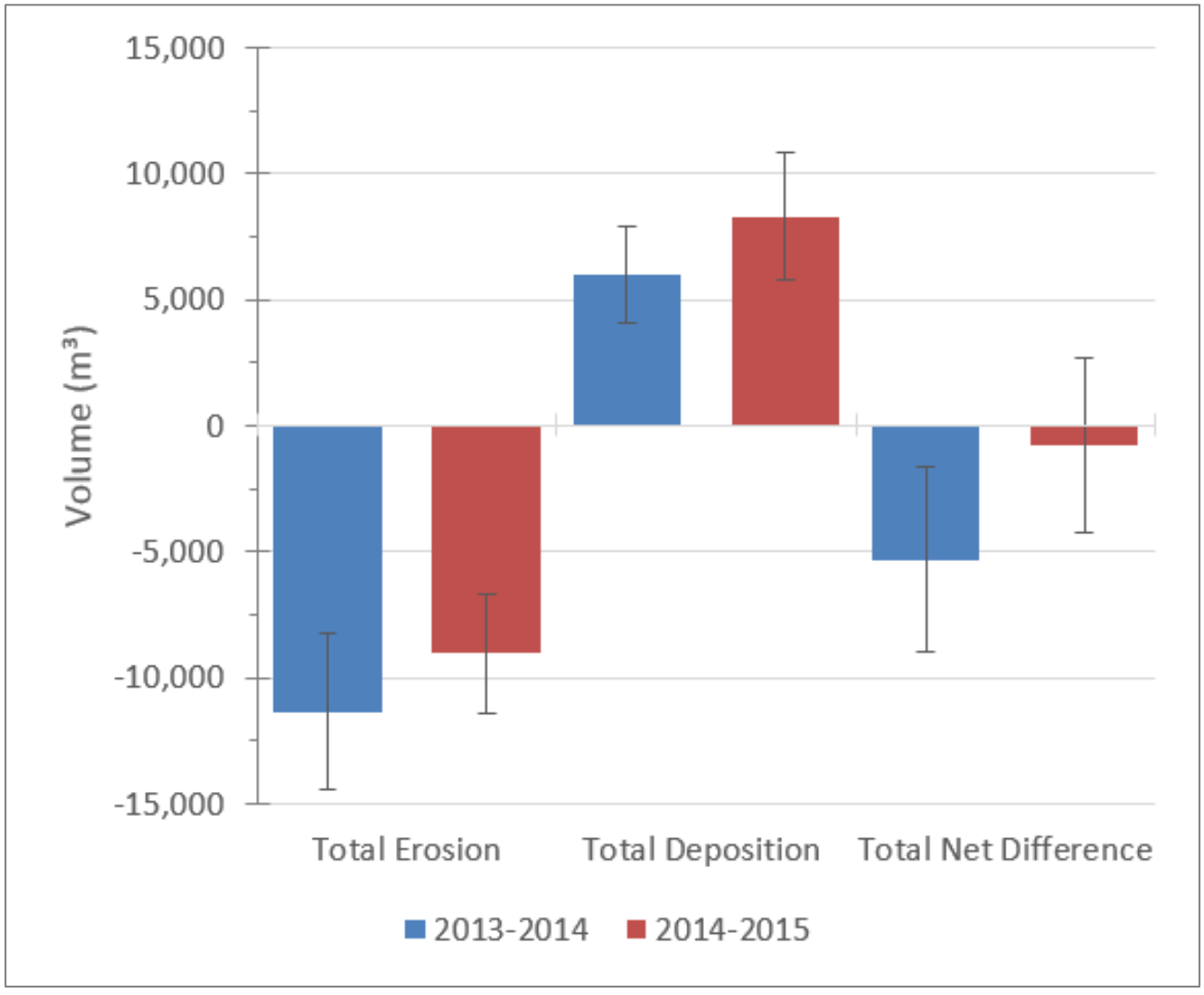

Figure 6: Volumetric sediment budget computed for the spatial intersection of the three datasets (see Table 5 for details).

Earth Surf. Dynam. Discuss., https://doi.org/10.5194/esurf-2017-38
Manuscript under review for journal Earth Surf. Dynam.
Discussion started: 29 June 2017

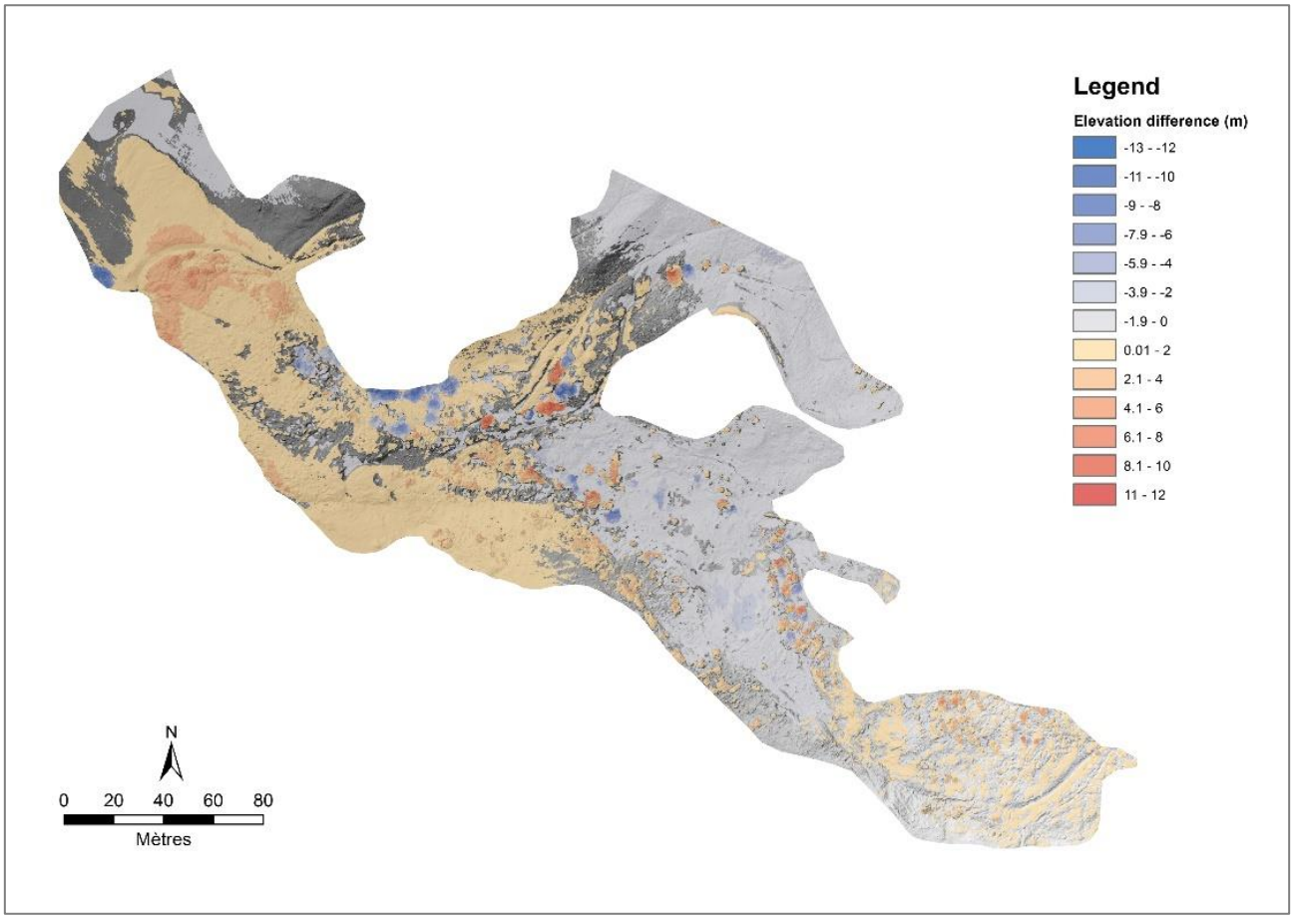

Figure 7: Elevation difference between two topographic reconstructions for the time interval June 2014 - October 2015.

Earth Surf. Dynam. Discuss., https://doi.org/10.5194/esurf-2017-38
Manuscript under review for journal Earth Surf. Dynam.
Discussion started: 29 June 2017

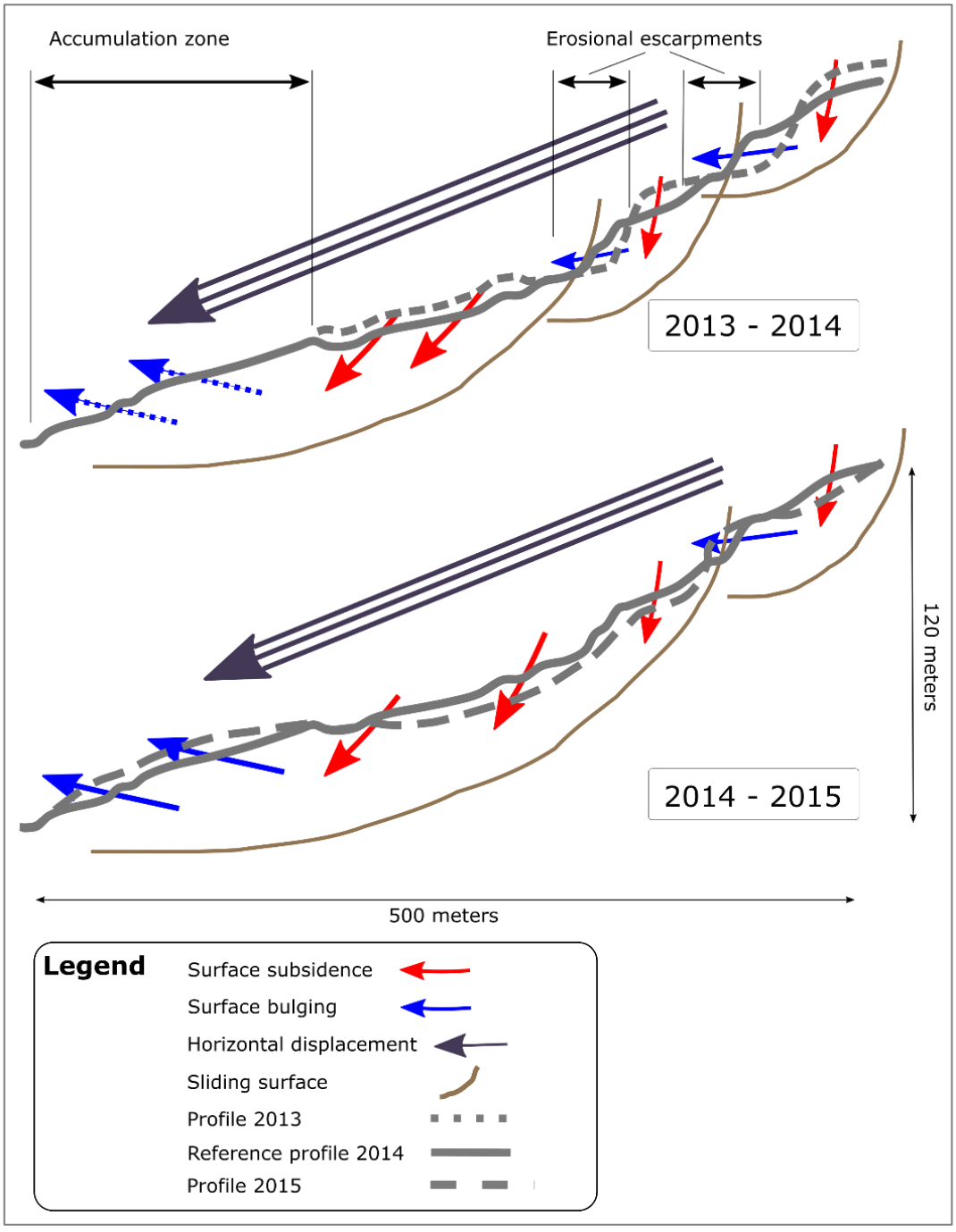

Figure 8: Schematic summary of the internal dynamics of the Schimbrig earthflow based on very-high resolution monitoring using the UAV-SfM framework.

Earth Surf. Dynam. Discuss., https://doi.org/10.5194/esurf-2017-38
Manuscript under review for journal Earth Surf. Dynam.
Discussion started: 29 June 2017

Tables

Table 1: Characteristics and accuracy assessment of 3D point cloud reconstructions. Root mean square errors (RMSE) are the standard deviation of differences between the coordinates of the ground control points, i.e. georeferencing targets, measured by GPS and the coordinates of these points within the 3D point clouds after georeferencing. Horizontal RMSE is computed by taking the horizontal components of the point coordinates while the vertical RMSE is computed by taking only the z component of point coordinates.

		October 2013	June 2014	October 2015
Point cloud characteristics	**Nb of pictures**	1143	4519	2501
	Nb of GCPs	49	108	99
	Area (ha)	5.86	17.69	15.59
	Point density (pts/m²)	**1456**	**1270**	**1080**
RMSE (m)	**Horizontal**	0.23	0.20	0.20
	Vertical	0.06	0.05	0.08
	Total error	**0.24**	**0.20**	**0.22**

Table 2: Limit of detection values for temporal analyses (meters).

		2013 - 2014	2014 - 2015
Limit of Detection (m)	**Horizontal**	0.30	0.28
	Vertical	0.08	0.09
	Total	**0.31**	**0.30**

Table 3: Descriptive statistics of the distances between 3D point clouds (meters).

Area of interest	Time interval	Min.	1st Qu.	Median	Mean	3rd Qu.	Max.
Intersection	**2013-2014**	-20.7	-1.1	-0.6	-1.0	0.5	20.4
	2014-2015	-27.6	-1.0	-0.5	-0.7	0.7	27.0
Interval	**2014-2015**	-28.8	-0.9	-0.4	-0.4	0.8	27.0

Earth Surf. Dynam. Discuss., https://doi.org/10.5194/esurf-2017-38
Manuscript under review for journal Earth Surf. Dynam.
Discussion started: 29 June 2017

Table 4: Mean annual horizontal displacement (meters) computed from the 3D point clouds using the COSI-Corr algorithm.

Area of interest	Time interval	Min.	1st Qu.	Median	Mean	3rd Qu.	Max.
Intersection	**2013-2014**	0.5	1.8	3.7	8.9	13.1	40.2
	2014-2015	0.2	0.9	2.2	5.7	11.3	21.1
Interval	**2014-2015**	0.2	0.9	3.6	6.3	11.8	21.1

Table 5: Volumetric sediment budgets (cubic meters).

Area of interest	Time interval	Estimate	Total Volume of Erosion (m^3)	Total Volume of Deposition (m^3)	Total Net Volume of Difference (m^3)
Intersection	**2013-2014**	Minimum	-14,463	4,093	-8,994
		Best	-11,345	6,012	-5,333
		Maximum	-8,227	7,932	-1,671
	2014-2015	Minimum	-11,383	5,747	-4,212
		Best	-9,054	8,293	-762
		Maximum	-6,726	10,838	2,688
Interval	**2014-2015**	Minimum	-19,191	12,472	-4,199
		Best	-15,093	17,005	1,912
		Maximum	-10,994	21,539	8,024